rHSA-nanosheets was successfully observed in the three-dimensional images (Fig. 2 (b) and (c)), demonstrating the flexible and tough nature of the rHSA-nanosheets.

AFM analysis of rHSA-nanosheets

To establish the morphological detail and the thickness of the rHSA-nanosheets, the nanosheets on the patterned ODS-SAM were observed by atomic force microscopy (AFM). Figure 3 (A) shows a large-scale (90 μm x 90 μm) three-dimension AFM image of the rHSA-nanosheets. The rectangular patterns (10 μm x 30 μm) were vividly embossed by rHSA, and non-specific adsorption of rHSA was scarcely observed on the SiO_2 regions. From the AFM cross-sectional image, the thickness of the rHSA-nanosheets plus the ODS-SAM was estimated to be 6.6 $\pm$ 1.0 nm as shown in Figure 3 (B) and (C). On the other hand, the thickness of the ODS-SAM itself was estimated to be 2.1 $\pm$ 0.7 nm (data not shown). Based on the difference between both thicknesses, the thickness of the rHSA-nanosheets was calculated to be 4.5 $\pm$ 1.0 nm, which agrees with the dimensions of rHSA.

rHSA-nanosheets having hetero-surfaces

For fabrication of the rHSA-nanosheets having hetero-surfaces, we conjugated NBD-labeled latex beads to the obverse side of TRITC-labeled rHSA-nanosheets on ODS-SAM. After the rHSA-nanosheets were detached from the ODS-SAM by the surfactant treatment, the dispersion was put on the cover glass plate, and then the sheets were observed with a confocal laser scanning microscope. There were abundant rectangular rHSA-nanosheets in various conformations (10 μm x 30 μm). We focused on a sheet adopting a bent-form as shown in Fig. 4. When the rhodamine-labeled rHSA of the sheets was excited at 543 nm, the entire sheet turned red with a measured emission wavelength of over 570 nm as shown in Fig. 4 (a). On the other hand, NBD of the latex beads was excited at a wavelength of 458 nm and detected in the emission wavelength region from 500 to 530 nm. We observed that the majority of the surface of the sheets turned a yellow color, and the bent site of the nanosheet was quenched due to the fluorescent resonance energy transfer (FRET) effect from the NBD to the rhodamine as shown in Fig. 4 (b). When these pictures (a) and (b) were overlayed, the resulting picture (c) clearly showed the red and yellow hetero surfaces, suggesting that NBD-

labeled latex beads adhered to the reverse surface at the bent site of the rHSA-nanosheet. Finally, we observed the latex beads-conjugated rHSA-nanosheets on ODS-SAM using an SEM. Many latex beads were specifically conjugated to the obverse side of the rHSA-nanosheets. The contrast of the rHSA-nanosheet was clear and uniform in comparison with that of SiO_2 region as shown in Fig. 4 (e) and (f), suggesting that the rHSA-nanosheets were thin and flat.

DISCUSSION

The purpose of this paper is to propose a novel method to prepare free-standing biocompatible nanosheets having hetero-surfaces, as a new biomaterial, by a combination of four processes as shown in Fig. 1; [1] specific adsorption of rHSA molecules onto patterned hydrophobic ODS-SAM regions, [2] preparation of nanosheets of SH-rHSA via two-dimensionally disulfide cross-linking, [3] surface modification of the resulting nanosheets, [4] preparation of free-standing nanosheets by detachment from the ODS-SAM.

We selected hydrophobic octadecyltrimethoxysilane (ODS) having a terminal CH_3 group for the SAM. Wadu-Mestheige *et al.* reported that bovine serum albumin could be selectively adsorbed on the SAM regions having a terminal CH_3 in comparison with SAM regions having a terminal OH or COOH (26). Since the resulting water contact angle of the ODS-SAM was similar to that of the ODS-SAM in the previous reports (27, 28), we could confirm that the hydrophobic ODS-SAM was certainly constructed on the silicon oxide (Table 1). As a first step, we investigated the suitable conditions (pH and concentration) for rHSA adsorption onto the ODS-SAM. At pH 7.4, the rHSA molecules did not adsorb on the ODS-SAM as seen from the contact angle measurement (Table 1). At that pH, the charge of rHSA is negative because the isoelectric point of rHSA is 4.9. Above that pH, rHSA molecules have little hydrophobic interaction with ODS-SAM and repel each other electrostatically. Therefore, they favor remaining dissociated in the solution rather than to assemble onto the ODS-SAM, resulting in no change in the contact angle. At pH 5.0, near the isoelectric point of rHSA, the contact angle was significantly decreased, suggesting that the rHSA molecules were firmly adsorbed on the ODS-SAM. As described below in the final step, the water contact angle after the surfactant treatment was comparable to that of the ODS-

SAM before rHSA adsorption, indicating that the attractive force giving rise to the adsorption of rHSA on the ODS-SAM was hydrophobic interaction. These results are consistent with the previous reported experiments on albumin adsorption at pH 5.0 and influences the three-dimensional shape of the individual albumin adsorbed on the terminal CH_3 of SAM (29, 30). These previous studies reported on the adsorption mechanism of albumin onto the SAM as the following; the electrostatic repulsion among albumin molecules was decreased at pH 5.0 and the inter-protein interaction (mostly hydrophobic interaction) strengthened, thus the albumin immobilized on the SAM was more stable than individual proteins in the solution state.

Next, at pH 5.0 and r.t., we explored the optimum concentration of the TRITC-labeled SH-rHSA adsorbed on the patterned ODS-SAM. In the case of the TRITC-labeled SH-rHSA at a concentration of 10 μg/mL or over, the rectangular patterns were distinctly stained by fluorescence, however, the SH-rHSA molecules were non-specifically adsorbed on the hydrophilic silicon oxide regions and brightened the background (data not shown). In the case of the SH-rHSA at a concentration of 0.1 μg/mL, the ODS patterns were hardly stained (data not shown). At the concentration of 1 μg/mL, almost all the ODS patterns were selectively stained (Fig. 2) and the rHSA molecules were predominantly located in the patterned ODS region (Fig. 3). The number of the ODS patterns arranged on the substrate (1 cm x 1 cm) is estimated to be approximately 6.7×10^4, and the number of rHSA molecules adsorbed on one patterned ODS region was calculated to be approximately 1.2×10^7 molecules, if the average surface area of one rHSA molecule is 25.5 nm^2 (31), and rHSA molecules are closely packed in the patterned ODS region (rectangular patterns: 10 μm x 30μm, area: 3.0×10^8 nm^2). Accordingly, the total number of the rHSA molecules adsorbing on the ODS patterns was calculated to be approximately 8.0×10^{11} molecules. Approximately 9% of the total rHSA was estimated to be adsorbed onto the ODS regions by immersing the substrate in the 1 mL rHSA solution at a concentration of 1 μg/mL, containing 9.0×10^{12} rHSA molecules. This was also supported by the results obtained from the other patterns such as circles and squares (data not shown). Consequently, we set the conditions of the rHSA adsorption onto the patterned ODS-SAM at pH 5.0, at r.t. and the concentration of 1 μg/mL.

The second step of the process is to cross-link each SH-rHSA molecule adsorbed on the patterned ODS-SAM to prepare nanosheets. We presumed that once the SH-rHSA molecules were adsorbed onto the substrate they would closely pack in the pattern, and thus be easy to cross-link in comparison with those in an aqueous solution. We utilized the cross-linking conditions for SH-rHSA in an aqueous solution to estimate the necessary conditions for cross-linking on the ODS-SAM. Cross-linking of the SH-rHSA by *N*-succinimidyl 3-(2-pyridyldithio) propionate (SPDP, spacer length is 0.68 nm), which has a terminal succinimidyl group and a pyridyldisulfide group to introduce the SH group to the surface of rHSA molecule after a DDT treatment, failed probably because the spacer length of SPDP would be too short to cross-link. Referring to a report by Komatsu *et al.*, where a dimer and clusters of rHSA had been exquisitely synthesized using a bis-maleimidohexane and an LC-SPDP, which have spacer lengths of 1.61 and 1.57 nm, respectively (31, 32), we used the LC-SPDP, which has similar functionality as that of SPDP. Only a small proportion of the SH-rHSA molecules cross-link at pH 7.4 in the presence of copper ion (II) as described in a previous report (25), suggesting that the rHSA molecules electrostatically repel each other because of the negative ζ-potential of the rHSA molecule. At pH 5.0, near the isoelectric point (pI = 4.9), the SH-rHSA was significantly cross-linked. The percentage of the peak areas of the void fractions for the total peak areas, which corresponded to the amount of the cross-linked rHSA over the molecular weight of 670 kDa, increased with the increasing number of the SH groups bound to one rHSA molecule. On the other hand, the cross-linking of the SH-rHSA was extremely slow in the absence of copper ion (II). The thiol oxidation is commonly facilitated in alkaline conditions because of complexation of copper ion (II) with thiolate anions (25). However, we used the weakly acidic conditions (pH 5.0), where the reaction rate was considered to be slow, suggesting that the thiol oxidation of the rHSA molecules would be controlled by electrostatic repulsion and hydrophobic interaction of rHSA molecules. Based on the above results, we could cross-link the SH-rHSA molecules adsorbed on the patterned ODS-SAM at pH 5.0 in the presence of 1 μM copper ion (II).

We measured the thickness of the rHSA-nanosheets as 4.5 $\pm$ 1.0 nm from the thickness of the ODS-SAM alone and the rHSA-nanosheet adsorbed on the ODS-SAM using AFM (Fig. 3). Carter *et al.* reported that the tertiary structure of the HSA molecule

determined from X-ray diffractometry could be described as a heart-shaped or equilateral triangular molecule with each side 8 nm in length and with an average thickness of 3 nm (33). The result showed that the rHSA-nanosheets could be regarded as a monolayer of SH-rHSA. As the hydrophobic interaction of SH-rHSA molecules with ODS-SAM should be stronger than that of SH-rHSA molecules with each other, the rHSA molecules weakly adsorbed onto the rHSA monolayer could be removed by washing before the addition of copper ion (II) as a catalyst of disulfide cross-linking. Furthermore, we confirmed that the non-specific adsorption onto the SiO_2 surface was extremely reduced if the substrate were immersed into the rHSA solution under the above conditions, based on the results obtained by AFM as well as fluorescent microscopy.

In the third step, we tried to modify the surface of the resulting nanosheet with latex beads, which were useful carriers because of their uniform size and ease of confirmation by microscopic observation. We conjugated the NBD-labeled latex beads onto the obverse side of the TRITC-labeled rHSA-nanosheets which had been adsorbed on the ODS-SAM and demonstrated the preparation of nanosheets having hetero surfaces. As shown in Fig. 4, there were many rHSA-nanosheets in various conformations of rectangles, such as bent-forms. Surprisingly, there were no broken sheets, suggesting that the rHSA-nanosheets are tough and extremely flexible. Focusing on the nanosheet having a bent-form (Fig. 4), when the rhodamine-labeled sheets were excited at 543 nm, the entire sheet turned red with a measured emission wavelength of over 570 nm (Fig. 4 (a)). On the other hand, we tried to detect the NBD on the surface of the sheet as yellow at the excitation of 458 nm and at the emission wavelength region from 500 to 530 nm. We could observe that the obverse surface of the sheet colored yellow, and the reverse side (bent site) was significantly quenched (Fig. 4 (b)). Since the FRET efficiency is related to the inverse six power of the distance between the acceptor and donor probes, the technique is elegantly used to measure the molecular distance at the 1.5-7.5 nm range (34, 35). Based on the above information and judging from the thickness of the rHSA-nanosheet, the quenching of the NBD emission from the bent-side of the nanosheet was caused by the FRET effect from NBD to rhodamine. It also indicates that the NBD-latex beads are attached only to the obverse side of the nanosheet. If a sufficient amount of the NBD-latex beads were attached to both sides of the sheet, then both sides of the

sheet would be quenched. Furthermore, we also confirmed that the latex beads were specifically conjugated to the obverse side of the rHSA-nanosheets using an SEM (Fig. 4 (e) and (f)). The nanosheets released from the substrate after conjugating the latex beads were heterogeneously modified.

In the final step, we investigated a method to detach the rHSA-nanosheets from the patterned ODS-SAM. We selected $C_{12}E_{10}$ as a non-ionic surfactant for which surfactant ability was independent of pH change. As shown in Table 1, when the substrate, to which rHSA (non SH modification) molecules were adsorbed, was immersed into a 1% (v/v) solution of $C_{12}E_{10}$ for 1 hr at r.t., the water contact angle was returned to that of the ODS-SAM before rHSA adsorption. This indicated that the rHSA adsorbed on the ODS-SAM was detached by the addition of a $C_{12}E_{10}$, and the attractive force giving rise to the adsorption of rHSA on the ODS-SAM was hydrophobic interaction. In the first and second processes, the SH-rHSA molecules were selectively adsorbed onto the patterned ODS regions and cross-linked in the presence of copper ion (II) to prepare the rHSA-nanosheets. Very few of the resulting nanosheets were detached from the substrate by immersion in the 1% $C_{12}E_{10}$ solution for 1 hr, whereas the control rHSA could simply detach. It took at least 6 hrs to detach the nanosheet from the substrate with the 1% $C_{12}E_{10}$ solution. On the other hand, we also conformed that the nanosheets were completely dissolved after 1 hr by a DTT treatment (data not shown). This suggested that it was difficult for the $C_{12}E_{10}$ molecules to diffuse into the spaces between the nanosheets and the ODS-SAM substrate, because the nanosheet was composed of sufficiently two-dimensionally cross-linked rHSA by intermolecular oxidation of thiol groups. Furthermore, we confirmed that the resulting rHSA-nanosheets were stable in the presence of $C_{12}E_{10}$ because the sheet shapes did not change after the $C_{12}E_{10}$ removal by dialysis (data not shown).

Using a confocal laser scanning microscopy, we fortunately observed the rHSA-nanosheets in three-demensional images and confirmed them to be a curved-form (Fig. 2 (c), and figure of supporting information). Based on analyses of quartz crystal microbalance (QCM) and grazing angle infrared spectroscopy (GA-FTIR) Roach *et al.* reported that albumin had enough adsorption affinity toward the hydrophobic (CH_3 terminus) compared to the hydrophilic surface (OH terminus), to cause adsorption-induced deformation (36).

Furthermore, Zheng *et al.* showed through modeling that the orientation of the adsorbed protein (lysozyme) was dependent on the discrete organization of the functional groups presented on the SAM surface, and in the case of the hydrophobic CH_3 group, hydrophobic amino residues of the protein were closest to the surface (37). From these references, we suggested that the rHSA-nanosheets would adopt a curved-form because the wettability of the obverse and reverse surface of the rHSA-nanosheets was different, that is, the obverse surface appeared to be more hydrophilic than the reverse surface. Consequently, we succeeded in the detachment of the rHSA-nanosheets from the ODS-SAM by mild conditions such as surfactant immersion in order to obtain uniform rHSA-nanosheets.

CONCLUSIONS

We succeeded in the preparation of free-standing rectangular (10 x 30 μm) and ultra-thin (4.5 ± 1.0 nm) rHSA-nanosheets by two-dimensional cross-linking via disulfide bonds on a patterned ODS-SAM, and could also obtain free-standing rHSA-nanosheets having hetero-surfaces by surface modification with fluorescent latex beads. Thus, the rHSA-nanosheets may be a suitable candidate as a new biomaterial for drug delivery carriers, hemostatic reagents and wound dressing for burn injury etc.. In our future work, we are preparing the rHSA-nanosheets on a large scale to carry the recombinant fragments of platelet membrane protein and/or dodecapeptides such as GPIbα and H12 to evaluate their performance *in vitro* and *in vivo*.

REFERENCES

(1) Tomii Y. Lipid formation as a drug carrier for drug delivery. Cur Pharma Design 2002;8:467-474.

(2) Takeoka S, Teramura Y, Okamura Y, Handa M, Ikeda Y, Tsuchida E. Fibrinogen-conjugated albumin polymers and their interaction with platelets under flow conditions. Biomacromolecules 2001;2:1192-1197.

(3) Takeoka S, Teramura Y, Ohkawa H, Ikeda Y, Tsuchida E. Conjugation of von Willebrand factor-binding domain of platelet glycoprotein Ibα to size-controlled albumin microsheres. Biomacromolecules 2000;1:290-295.

(4) Teramura Y, Okamura Y, Takeoka S, Tsuchiyama H, Narumi H, Kainoh M, Handa M. Ikeda Y, Tsuchida E. Hemostatic effects of polymerized albumin particles bearing rGPIa/IIa in thrombocytopenic mice. Biochem Biophys Res Commun 2003;306:256-260.

(5) Okamura Y, Takeoka S, Teramura Y, Maruyama Y, Tsuchida E, Handa M, Ikeda Y. Hemostatic effects of fibrinogen-γ chain dodecapeptide-conjugated polymerized albumin particles *in vitro* and *in vivo*. Transfusion 2005;45:1221-1228.

(6) Takeoka S, Teramura Y, Okamura Y, Tsuchida E, Handa M, Ikeda Y. Rolling properties of rGPIbα-conjugated phospholipid vesicles with different membrane flexibilities on vWf surface under flow conditions. Biochem Biophys Res Commun 2002;296:765-770.

(7) Okamura Y, Ippei M, Teramura Y, Maruyama Y, Tsuchida E, Handa M, Ikeda Y, Takeoka S. Hemostatic effects of phospholipid vesicles carrying fibrinogen-γ chain dodecapeptide *in vitro* and *in vivo*. Bioconjugate Chem 2005;16:1589-1596.

(8) Okamura Y, Handa M, Suzuki H, Ikeda Y, Takeoka S. New strategy of platelet substitutes for enhancing platelet aggregation at high shear rates; cooperative effects of a mixed system of fibrinogen γ-chain dodecapeptide- or glycoprotein Ibα-conjugated latex beads under flow conditions. J Artif Organs 2006;9:251-258.

(9) Takeoka S, Okamura Y, Teramura Y, Watanabe N, Suzuki H, Tsuchida E, Handa M, Ikeda Y. Function of fibrinogen γ-chain dodecapeptide-conjugated latex beads under flow. Biochem Biophys Res Commun 2003;312:773-779.

(10) Mattson J, Forrest JA, Borjesson L. Quantifying glass transition behaviour in ultrathin free-standing polymer films. Phys Rev E 2000;62:5187-5200.

(11) Tang Z, Kotov NA, Magonov S, Ozturk B. Nanostructured artificial nacre. Nat Mater 2003;2:413-418.

(12) Mallwitz F, Laschewsky A. Direct access to stable, freestanding polymer membranes by layer-by-layer assembly of polyelectrolytes. Adv Mater 2005;17:1296-1299.

(13) Mamedov A, Kotov NA, Prato M, Guldi DM, Wicksted JP, Hirsch A. Molecular design of strong single-wall carbon nanotube/polyelectrolyte multiplayer composites. Nature Mater 2002;1:190-194.

(14) Huck WT, Stroock AD, Whitesides GM. Synthesis of geometrically well-defined, molecularly thin polymer films. Angew Chem Int Edn 2000;39:1058-1061.

(15) Mamedov A, Kotov N. Free-standing layer-by-layer assembled films of magnetite nanoparticles. Langumuir 2000;16:5530-5533.

(16) Mallwitz F, Goedel WA. Physically cross-linked ultrathin elastomeric membranes. Angew Chem Int Edn 2001;40:2645-2647.

(17) Eck W, Küller A, Grunze M, Völkel B, Gölzhäuser A. Freestanding nanosheets from crosslinked biphenyl self-assembled monolayers. Adv Mater 2005;17:2583-2587.

(18) Xu H, Goedel WA. Polymer-silica hybrid monolayers as precursors for ultrathin free-standing porous membranes. Langumuir 2002;18:2363-2367.

(19) Nardin C, Winterhalter, M, Meier W. Giant free-standing ABA triblock copolymer membranes. Langumuir 2000;16:7708-7712.

(20) Ulman A. An introduction to ultrathin organic films from langmuir-blodgett to self-assembly. Academic press: San Diego, CA, 1991.

(21) Khoshtariya DE, Wei J, Liu H, Yue H, Waldeck DH. Charge-transfer mechanism for cytochrome *c* adsorbed on nanometer thick films. Distinguishing frictional control from conformational gating. J Am Chem Soc 2003;125:7704-7714.

(22) Ferapontova EE, Shipovskov S, Gorton L. Bioelectrocatalytic detection of theophylline at theophylline oxidase electrodes. Biosens Bioelectron 2007;22:2508-2515.

(23) Niwa D, Yamada Y, Homma T, Osaka T. Formation of molecular templates for fabricating on-chip biosensing devices. J Phys Chem B 2004;108:3240-3245.

(24) Sugimura H, Ushiyama H, Hozumi A, Takai O. Micropatterning of alkyl- and fluoroalkylsilane self-assembled monolayers using vacuum ultraviolet light. Langmuir 2000;16:885-888.

(25) Cavallini D, De Marco C, Dupre S, Rotilio G. The copper catalyzed oxidation of cysteine to cystine. Arch Biochem Biophys 1969;130:354-361.

(26) Wadu-Mestherige K, Amro NA, Liu GU. Immobilization of proteins on self-assembled monolayers. Scanning 2000;22:380-288.

(27) Siqueira PDF, Wenz G, Schunk P, Schimmel T. An improved method for the assembly of amino-terminated monolayers on SiO_2 and the vapor deposition of gold layers. Langmuir 1999;15:4520-4523.

(28) Depalma V, Tillman N. Friction and wear of self-assembled trichlorosilane monolayer films on silicon Langmuir 1989;5:868-872.

(29) Norde W, Giesbers M, Pingsheng H. Langmuir-Blodgett films of polymerized 10,12-pentacosadiyonic acid as substrates for protein adsorption. Colloids Surf B 1995;5:255-263.

(30) Prime KL, Whitesides GM. Adsorption of proteins onto surfaces containing end-attached oligo(ethylene oxide): A model system using self-assembled monolayers. J Am Chem Soc 1993;115:10714-10721.

(31) Komatsu T, Oguro Y, Teramura Y, Takeoka S, Okai J, Anraku, M, Otagiri M, Tsuchida E. Physicochemical characterization of cross-linked human serum albumin dimer and its synthetic heme hybrid as an oxygen carrier. Biochim Biophys Acta 2004;1675:21-31.

(32) Komatsu T, Oguro Y, Nakagawa A, Tsuchida E. Albumin clusters: structurally defined protein tetramer and oxygen carrier including thirty-two iron (II) porphyrins. Biomacromolecules 2005;6:3397-3403.

(33) Carter DC, Ho JX. Structure of serum albumin. Adv Protein Chem 1994;45:153-204.

(34) Stryer L, Haugland RP. Energy transfer: a spectroscopic ruler. Proc Natl Acad Sci USA 1967;58:719-726.

(35) Stryer L. Fluorescence Energy Transfer as a Spectroscopic Ruler. Ann Rev Biochem 1978;47:819-946.

(36) Roach P, Farrar D, Perry CC. Interpretation of protein adsorption: surface-induced conformational changes. J Am Chem Soc 2005;127:8168-8173.

(37) Zeng J, Li L, Chen S, Jiang S. Molecular simulation study of water interactions with oligo (ethylene glycol)-terminated alkanethiol self-assembled monolayers. Langmuir 2004;20:8931-8938.

FIGURE CAPTIONS

Fig. 1 Preparation of free-standing rHSA-nanosheets having hetero-surfaces on the patterned ODS-SAM.

Fig. 2 **(a)** Observation of SH-rHSA adsorbed onto the patterned ODS-SAM using fluorescent microscopy. **(b)** Observation of the free-standing rHSA-nanosheets detached from the patterned ODS-SAM and **(c)** the 90° rotation image of **(b)** using confocal laser fluorescent microscopy.

Fig. 3 AFM images of rHSA-nanosheets adsorbed onto the patterned ODS-SAM. **(a)** 3-D image, **(b)** top view image, **(c)** cross-sectional image.

Fig. 4 Confocal laser scanning microscopic images of rhodamine-labeled rHSA-nanosheets, of which the obverse sides were modified with NBD-labeled latex beads. **(a)** Rhodamine-conjugated rHSA was exited at a wavelength of 543 nm, and the emission wavelength detected at over 570 nm, **(b)** NBD conjugated latex beads were excited at a wavelength of 458 nm and the emission wavelength detected at 500 to 530 nm, **(c)** the overlayed image of **(a)** and **(b)**, and **(d)** Schematic image of rhodamine-labeled rHSA-nanosheets, of which the obverse sides were modified with NBD-labeled latex beads. **(e)** SEM image of rHSA-nanosheets, of which the obverse sides were modified with latex beads, **(f)** magnified SEM image of (e).

Table 1 Water contact angles of ODS-SAM before and after rHSA adsorption

rHSA adsorption		water contact angle (degree)
before		83 ± 1
after	pH 5.0	67 ± 1
	pH 7.4	80 ± 2
[a] $C_{12}E_{10}$		82 ± 1

(a) $C_{12}E_{10}$ was added to the ODS-SAM after rHSA adsorption at pH 5.0, incubated at r.t. for 1 hr and then washed with distilled water.

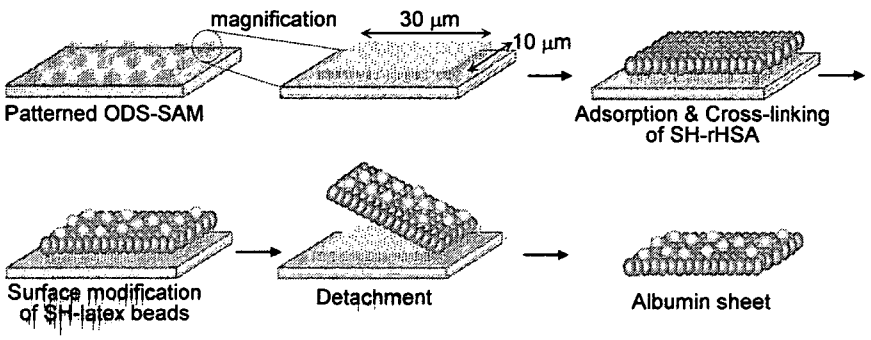

Figure 1 Okamura Y et al.

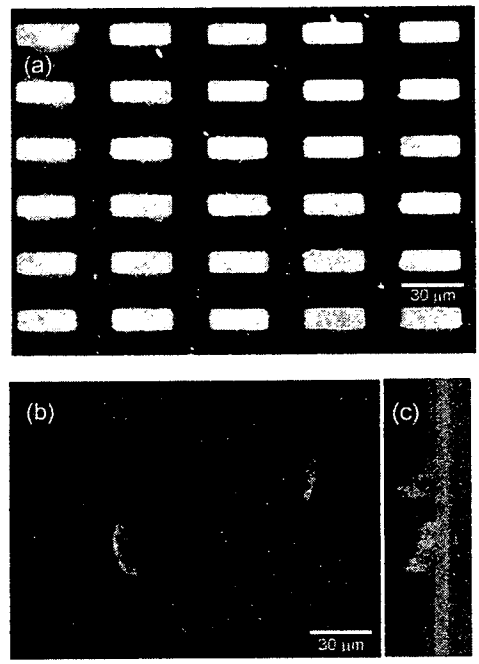

Figure 2 Okamura Y et al.

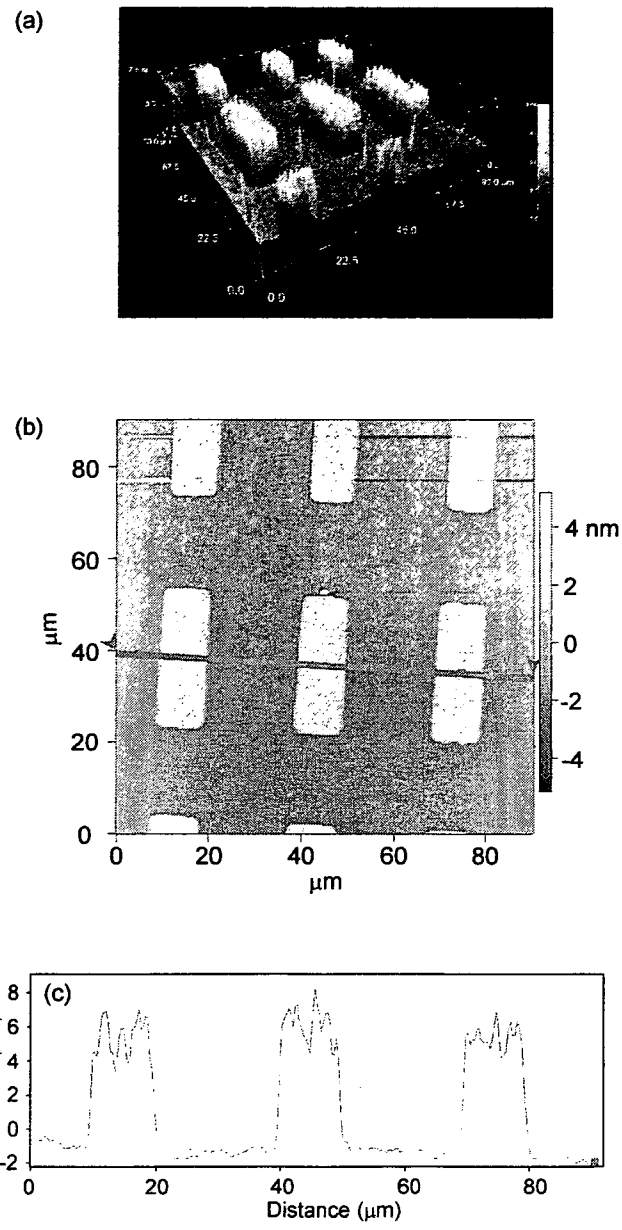

Figure 3 Okamura Y et al.

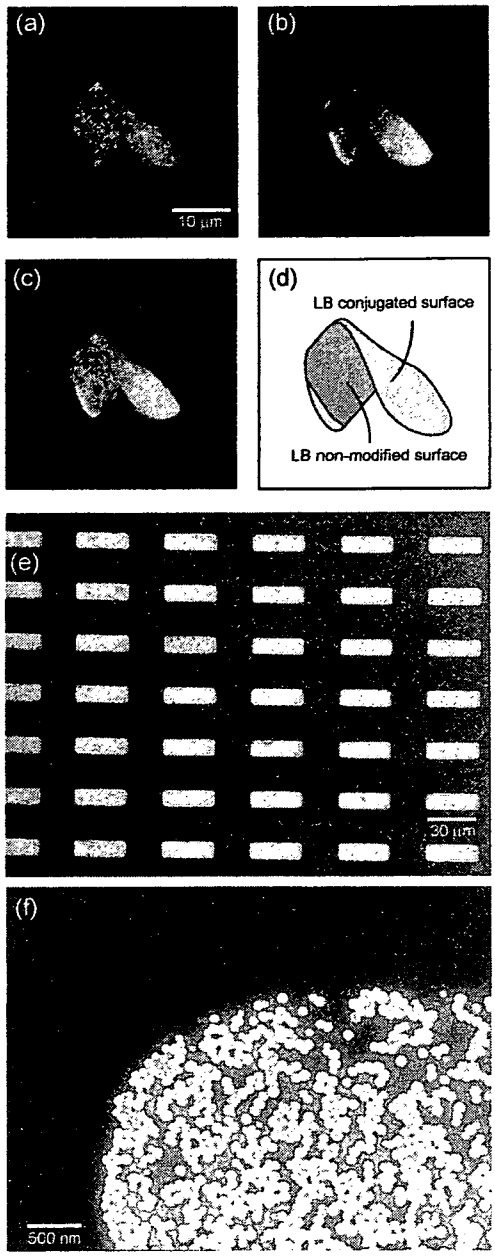

Figure 4 Okamura Y et al.

Brief report

Three-dimensional imaging of growing thrombus *in vivo*

Takayuki Morikawa[1], Mayumi Kajimura[1], Mio Ichikawa[1], and Makoto Suematsu[1].

[1] Department of Biochemistry and Integrative Medical Biology, Keio University School of Medicine, Tokyo160-8582, Japan.

Running title: Real-time imaging of thrombus formation

KEY WORDS: thrombus formation, three-dimensional reconstruction, confocal, real-time, intravital microscopy

Address for Correspondence and Galley Proofs:
Mayumi Kajimura
Department of Biochemistry and Integrative Medical Biology
Keio University School of Medicine,
35 Shinano-machi, Shinjuku-ku,
Tokyo, 160-8582, Japan
Phone: +81-3-3353-1211 (extension 63915)
Fax: +81-3-3358-8138
E-mail: myk30@sc.itc.keio.ac.jp

ABSTRACT

Although several methods have been developed to investigate thrombus or hemostatic plug formation in microvessels *in vivo*, our knowledge on platelet behavior during such a process is still limited. We, therefore, developed new instrumentation which enables us to induce interactions of individual platelets and to detect their behavior with endothelium in and around the growing thrombus. To evoke a platelet reaction, focal hemorrhage was induced with a nitrogen-dye laser focused through the microscope optics using mesenteric microcirculation of the rat. Platelet deposition at the site of injury was then observed during thrombus formation in real-time. The system was able to provide images with high spatial resolution at video-frame rate that could be used to reconstruct three-dimensional model of a thrombus. (Abstract movie)

INTRODUCTION

Process of thrombus or normal hemostatic plug formation upon vascular injury is initiated by the activation of circulating platelets. Biological and rheological properties of platelets have been extensively studied in the experimental systems *in vitro* such as in a parallel-plate flow chamber. Because platelet responses are affected by many factors in the normal environment, such as endothelium, other circulating cells, and blood flow *per se*, it is inevitable to examine such interactions *in vivo*. In this regard, several methods have been developed to evoke platelet activation and to observe thromboembolic process *in vivo* [1-3]. Among these, the most recent technology was developed by Falti *et al.* [3] with which vascular injury is induced by laser ablation technology and high-speed, near simultaneous acquisition of images of multiple fluorescent probes and the three-dimensional reconstruction of thrombus were made possible. Here we describe a new intravital imaging system that is essentially a modified technique of Falti *et al.* [3]. Because the system utilizes an analog 3CCD camera without using binning function, it was possible to acquire the image in real-time, i.e. 3 x 640 x 480 pixels format, 30 frames s^{-1} which enabled us to evaluate a single platelet behavior *in situ*.

MATERIALS AND METHODS

Preparation of rats for intravital microscopy

Experiments were approved by the local ethical committee on the use of laboratory animals. Male Wistar rats (250-280 g; Clea Japan, Tokyo) were anesthetized with an intramuscular injection of sodium pentobarbital at 50 mg kg^{-1}, and the femoral vein was cannulated with a polyethylene catheter. Platelets circulating *in vivo* were labeled with an intravenous injection of carboxyfluorescein diacetate succinimidyl ester (CFDA-SE,

Molecular Probes, Inc., Eugene, OR, USA) as described previously [4,5]. This compound is membrane-permeable and after it has entered cells it is hydrolyzed by esterase which predominantly occurs in platelets and leukocytes. After the dye infusion, the abdomen was opened and the ileocecal portion of the mesentery was arranged on the surface of the glass-coverslip for intravital observation. The mesentery was superfused continuously with the Krebs-Henseleit buffer saturated with 95% N_2/5% CO_2 at 2.0 ml min^{-1} at 37□C.

Thrombus generation by laser ablation of microvascular walls

Either an arteriole or a venule was chosen and endothelial injury was induced by a pulsed nitrogen-dye laser at 440 nm applied through the microscope objective using the MicroPoint laser system [3]. Arterioles with a diameter of 15-30 μm or venules with that of 20-35 μm were targets for the injury.

Intravital imaging of thrombus formation

The imaging system constructed in this study is a modified method of Falati *et al.* [3]. The system was developed around an Olympus BX51W1 up-right microscope with a trinocular head (Olympus, Inc., Tokyo, Japan). Applications of the intravital microscopy in these experiments require either a 40 x (LUMPlanFI/IR, NA 0.8) or a 60 x (LUMFL, NA 1.1) water immersion lens. For confocal microscopy, we used a Yokogawa CSU21 confocal scanner (Yokogawa, Inc., Saitama, Japan) based on Nipkow disk technology. This confocal scanner uses the same pinholes for entrance and exit light beams but is also equipped with a second rotating disk that contains approximately 20,000 pinholes, each with a microlens. The disks rotate together at 1,800 rpm so that the light beams raster-scan the specimen. This technology allows the system to capture up to 360 flashed-frames s^{-1}. An argon-krypton two-line laser (Melles Griot, Carlsbad, CA, USA) provides the fluorescent light for confocal microscopy with excitation at 488 nm and 568 nm. The objective lens was mounted on a piezoelectric driver (Physik Instrumente-PZ73E, PI-Polytec CO., Ltd, Tokyo, Japan) which was controlled by a function generator (SG-4105, Iwatsu, Tokyo, Japan). A schematic representation of the instrumentation is shown in Figure 1.

To generate a laser-induced thrombus, the system was fitted with a nitrogen ablation laser (MicroPoint, Photonic Instruments, St. Charles, IL, USA) which was introduced via the epi-illumination port and was focused on the specimen through the microscope objectives. The output of the laser was at 337 nm but was subsequently tuned through a dye cell. We used coumarin as dye, which emits at 440nm. The laser delivers 4-nsec energy pulses, at a frequency between 3 and 10 Hz, over a surface approximately 1-μm in diameter; the energy of the pulses can be controlled by the operator. In order to conduct consistent ablation, the

objective lens was kept at a stationary position until we became certain about a successful ablation. The ablation was considered successful if erythrocytes left from the vessel, indicating that all components of the vessel layers were damaged. We then started to operate a piezoelectric driver which allows very fine movement in the vertical direction of the sample.

Figure 1

Video acquisition and three-dimensional reconstruction of developing thrombus

The central part of the trinocular stand was connected to an analog color CCD camera (JK-TU52H, Toshiba, Tokyo) that allowed us to record color images with acceptable spatial and temporal resolutions (640 x 480 pixels format, 30 frames s^{-1}). Analog signals were digitized via a frame grabber (Meteor-II, Matrox Electronic Systems Ltd, Tokyo). The computer had a 3 GHz processor, 1 GB of RAM, and three SCSI hard drives including one 160GB-RAID-0. This computer system was capable to acquire real-time color images for the duration of approximately 90 min. Using a piezo-electric driver on an objective lens, optical slices are obtained. Imaging software (StreamPix ver. 3.7.0, Norpix Inc., Montreal, Quebec, Canada) was used to control the hardware components during image acquisition. Finally acquired images were stacked to generate a three-dimensional reconstruction of a developing thrombus by three kinds of imaging software; StreamPix, IP Lab (ver. 3.6.4, Scanalytics, Inc., Fairfax, VA, USA) and Vox Blast (ver. 3.0, VayTek, Inc., Fairfield, Iowa, USA).

RESULTS

Tissue depth of the formed images

Figure 2 shows a representative image of a three-dimensional reconstruction. Here we first positioned the microscope lens at the center of the venule, namely at the point where the largest diameter was seen. The position of the lens was then moved upwards by 22.5 μm and images composed of 640 x 480 pixels with 1.5-μm steps for the total depth of 45 μm were collected. The 45-μm height of the images was intentionally greater than the diameter of the venule in order to compensate for inexact positioning of the lens before the start of the experiment. As seen in Panel A of the x-z section which transverses to the microvessels on this mesentery, only the top half of the circumference of this venule, but not the bottom half of it was visualized. When the dissecting plane was moved 18.7-μm more deeply (Panel B), the shape of the platelet thrombus on this venular wall became apparent. However, when a further 18.3-μm deeper section was made (Panel C), the system failed to